Available online at www.sciencedirect.com
ScienceDirect
Trans. Nonferrous Met. Soc. China 31(2021) 2051−2061
Transactions of Nonferrous Metals Society of China
www.tnmsc.cn

Sb_2S_3 nanorods/porous-carbon composite from natural stibnite ore as high-performance anode for lithium-ion batteries

Qi WANG[1], Yan-qing LAI[1], Fang-yang LIU[1], Liang-xing JIANG[1], Ming JIA[1,2], Xi-lun WANG[3]

1. School of Metallurgy and Environment, Central South University, Changsha 410083, China;
2. Hunan Provincial Key Laboratory of All-Solid-State Energy Storage Materials and Devices, Hunan City University, Yiyang 413000, China;
3. Yiyang Huachang Antimony Industry Co., Ltd., Yiyang 413000, China

Received 9 July 2020; accepted 24 April 2021

Abstract: To avoid the high purity reagents and high energy consumption involved in the manufacturing of lithium-ion battery anode materials, Sb_2S_3 nanorods/porous-carbon anode was prepared by remodeling natural stibnite ore with porous carbon matrix via a simple melting method. Due to the nanostructure of Sb_2S_3 nanorods and synergistic effect of porous carbon, the Sb_2S_3 nanorods/porous-carbon anode achieved high cyclic performance of 530.3 mA·h/g at a current density of 100 mA/g after 150 cycles, and exhibited a reversible capacity of 130.6 mA·h/g at a high current density of 5000 mA/g for 320 cycles. This shows a great possibility of utilizing Sb_2S_3 ore as raw material to fabricate promising anodes for advanced lithium-ion batteries.

Key words: lithium-ion batteries; Sb_2S_3 ore; economical preparation; nanostructured anode material

1 Introduction

Lithium-ion batteries (LIBs), the generally known energy storage devices, have been extensively employed nowadays in portable electronic devices, electric vehicles, and smart grids [1,2]. Due to the high structure stability and cyclic performance, graphite has dominated in the current market of commercial anode materials [3]. However, this kind of anode with dissatisfactory specific capacity (372 mA·h/g) and sluggish ion intercalation kinetic is unbefited for next generation batteries that require high energy/power density [4,5]. Therefore, novel anode materials exhibiting high capacity, prominent cycle/rate performance, low cost, and good safety are urgently required. Among a considerable number of alternative anodes, metal sulfide materials have aroused rising attention over the past few years for their high specific capacity, suitable lithiation potential and more abundant reserves than those of natural graphite [6−8]. Antimony sulfide, i.e., the typical one, has been recognized as one of the most potential anode materials for LIBs on account of its high theoretical capacity of 946 mA·h/g and good electrochemical reversibility [9]. However, the commercialization of Sb_2S_3-based anodes has been limited by two defects. One is the significant volume change during the cycling, which will destroy the electrode structure; the other is the poor electron and ion conductivity, thereby inhibiting the diffusion of Li^+ and the transport of electron in bulk Sb_2S_3 [10].

To solve the mentioned problems, nanoscale Sb_2S_3 activity materials and Sb_2S_3 composited with conductive carbon were prepared to release strain and shorten the diffusion pathways of Li^+ and

Corresponding author: Ming JIA, Tel: +86-731-88830649, E-mail: jiamingsunmoon@aliyun.com
DOI: 10.1016/S1003-6326(21)65637-6

electron in the particles, as well as improve the electronic conductivity. However, the reported Sb_2S_3-based anode materials were largely synthesized with high-purity metal or metal salt as the raw materials, thereby inevitably extending the preparation duration and increasing the cost. Accordingly, in our previous report [11], a concept was proposed to prepare Sb_2S_3 anode with low cost and simple procedure, i.e., the direct use of natural stibnite ore as the initial raw material, and a simple vapor transport deposition was subjected to fabricate nanostructured Sb_2S_3 thin-film anode. The thin-film anode exhibited both high cyclic performance and rate property, demonstrating the possibility of high-performance electrodes fabricated directly from their ores without metallurgical treatment, and the potential economic significance of ore utilization. In this study, a novel Sb_2S_3 nanorods/porous-carbon anode was reported initially by remodeling natural stibnite ore with porous carbon matrix based on a simple melting method. By controlling the mass ratio of ore to porous carbon, different morphologies of remodeled Sb_2S_3 particle could be obtained (e.g., nanorods, micro-sheets, and microspheres) in the Sb_2S_3 ore/porous carbon anodes. The Sb_2S_3 nanorods/porous carbon anode exhibited excellent cycling performance and high rate capacity, which is promising for next generation of LIBs.

2 Experimental

2.1 Preparation of Sb_2S_3 nanorods/porous-carbon

Sb_2S_3 nanorods/porous-carbon was prepared with a simple melting method. First, a total mass of 5 g Sb_2S_3 ore (95 wt.% of Sb_2S_3, purchased from Hunan TAOJIANG BANXI Antimony Mine, China) and porous carbon with different mass ratios were mixed by ball milling to produce a mixture. In the mixing procedure, four groups of samples were prepared by regulating the mass ratio of Sb_2S_3 ore in the mixture, i.e., 50, 60, 70 and 80 wt.%. Subsequently, the corresponding four samples were placed in a quartz tube full of argon, and the tube was then heated up from ambient temperature to 600 °C at a rate of 5 °C/min, which was kept at 600 °C for 5 h. Before the heating, the tube was vacuumed to 0.07 MPa with a pump. The four samples after the melting process were termed as Melt-50%, Melt-60%, Melt-70% and Melt-80%, respectively. The 50 wt.% Sb_2S_3 ore mixture without melting treatment was termed as SO/PC-50%. Likewise, the porous carbon matrix was prepared as reported in the existing work of the authors [12].

2.2 Material characterizations

The crystal structures of the samples were investigated by using X-ray diffraction (XRD, Rigaku 3014). The morphologies and compositions of the samples were detected with field emission scanning electron microscopy (FE-SEM) and energy dispersive X-ray spectrometry (EDS), respectively. X-ray photoelectron spectroscopy (XPS, K_α) was used to analyze the elements state, and Raman measurements (Jobin-Yvon LabRAM HR800−Horiba spectrometer) were performed to characterize the bond properties. The specific surface area of the samples was tested via the Brunauer-Emmett-Teller (BET) method. Furthermore, the microstructure was observed with the transmission electron microscopy (TEM) and high-resolution transmission electron microscopy (HRTEM, JEOL JEM−2100).

2.3 Electrochemical measurements

To prepare the electrode, the active materials, Super P, and polyvinylidene fluorid with a mass ratio of 80:10:10 were mixed and homogeneously dispersed in N-methylpyrro-lidone. Subsequently, the slurry was cast onto a flat Cu foil and then dried at 60 °C overnight in a vacuum oven. The obtained electrodes were cut into disc with a diameter of 12 mm. Next, the mass loading of active material on the electrodes reached nearly 1.0−1.2 mg/cm^2. Then, CR2025 coin-type cells were assembled with Li foil as the counter and reference electrode, and microporous membrane Celgard 2400 as the separator. The electrolyte amount was 1 mol/L $LiPF_6$ in a mixed solution of ethylene carbonate (EC), dimethyl carbonate (DMC) and ethyl methyl carbonate (EMC) (1:1:1, volume ratio). Afterwards, based on a multichannel battery test system (LAND CT2001A), the cells were tested in the voltage range of 0.01−3 V. The cyclic voltammetry (CV) of the cells was performed on a VSP (Bio-Logic SAS) electrochemical workstation at a scanning rate of 0.1 mV/s under the voltage from 0.01 to 3.0 V (vs Li^+/Li). Electrochemical impedance spectroscopy

(EIS) measurements were conducted under the amplitude of 10 mV at the frequency from 100 kHz to 0.01 Hz.

3 Results and discussion

3.1 Phase structure and chemical composition

Figure 1(a) presents the XRD patterns of porous carbon, Sb_2S_3 ore and the four melted samples (Melt-50%, Melt-60%, Melt-70% and Melt-80%). A prominent peak was identified at 2θ=26.55° in porous carbon followed by four small peaks at 2θ=42.40°, 44.55°, 54.62° and 77.46°, which could be indexed to the standard XRD pattern of Graphite-2H (JCPDS No. 41-1487). In addition, the peaks of the Sb_2S_3 ore were well indexed to the stibnite (JCPDS No. 42-1393), except for a small peak at 2θ=26.57°, owing to the impurity of SiO_2 in the ore (JCPDS No. 81-0065). After the melting treatment was performed, the remodeled products of the four samples exhibited good crystallinity with stibnite phase (JCPDS No. 42-1393), which demonstrated a good chemical stability of Sb_2S_3 in the porous carbon matrix. Raman measurements were performed to analyze the band properties of the samples (Fig. 1(b)). Two typical intense peaks of porous carbon were identified at 1341.5 and 1594.7 cm^{-1}, belonging to the D-band and the G-band, respectively [13]. The I_D/I_G value represents the extent of the defects and the degree of graphitization of porous carbon [14], which reached 1.03, confirming that the porous carbon was partially graphitized. The graphitization property ensured the high conductivity of the carbon materials [15]. The Raman shift of Sb_2S_3 ore showed the intense peaks at 450.0, 299.5, 280.3, 250.1, 186.9, 146.3 and 107.6 cm^{-1}. The peaks at 299.5 and 280.3 cm^{-1} belonged to the Sb_2S_3 phase [16,17], and the others corresponded to the Sb_2O_3 [18,19]. The appearance of Sb_2O_3 bands might be attributed to the slight oxidation of the surface of Sb_2S_3 ore particles in the air, which was also reported in other works [20]. The typical Sb_2O_3 peaks at 450 and 250.1 cm^{-1} disappeared in the melted samples, and the strong peaks of Sb_2S_3 could be observed. During the melting process, the

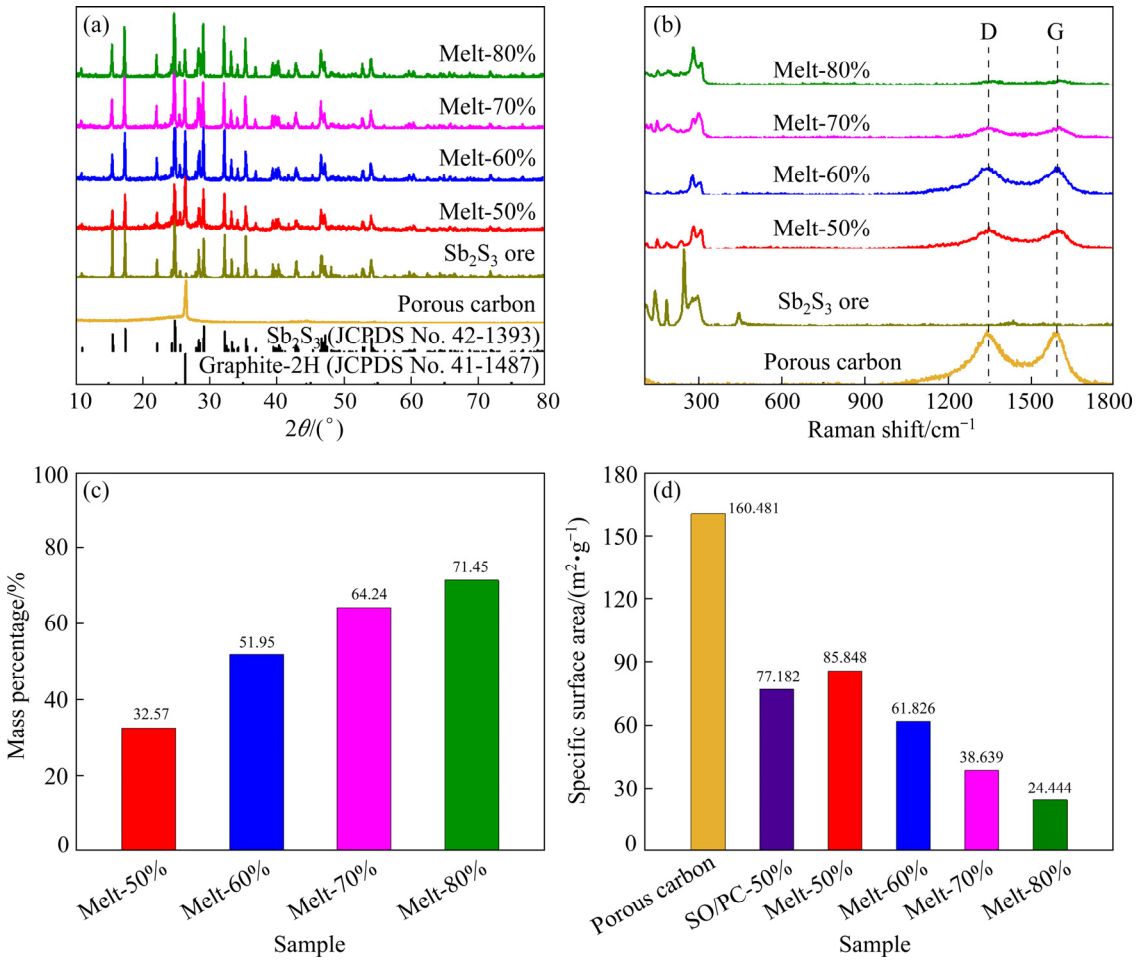

Fig. 1 XRD patterns (a), Raman shifts (b), Sb_2S_3 ore mass percentages (c), and specific surface areas (d) of samples

Sb_2S_3 ore evaporated partially and had a small amount of mass loss for its relatively low melting point (550 °C) and high vapor pressure, as well as the low pressure in the tube. For simplification, the mass loss of the samples after melting was assumed to be equal to the evaporated mass of Sb_2S_3 ore. Figure 1(c) presents the corresponding Sb_2S_3 mass ratios in the samples of Melt-50%, Melt-60%, Melt-70% and Melt-80%, reaching 32.57%, 51.95%, 64.24%, and 71.45%, respectively. Figure 1(d) illustrates the specific surface area of the samples. It is indicated that, the porous carbon displayed a high surface area of 160.481 m^2/g. With the increase of Sb_2S_3 ore content in the mixture, the specific surface area of samples was decreased after melting, which covered 85.848 m^2/g for Melt-50%, 61.826 m^2/g for Melt-60%, 38.639 m^2/g for Melt-70%, and 24.444 m^2/g for Melt-80%. Furthermore, the sample SO/PC-50% exhibited a surface area of 77.182 m^2/g, lower than Melt-50% but higher than Melt-60%, consistent with their mass percentages of Sb_2S_3 ore.

The morphologies of porous carbon and Sb_2S_3 ore were further investigated by using the FE-SEM. The porous carbon presented a honeycomb-like shape with a pore diameter of nearly 140 nm and a wall thickness of approximately 7 nm, and the pore structures interconnected with each other, forming bulk graphitized carbon material (Fig. 2(a)). The Sb_2S_3 ore displayed an uneven particle size

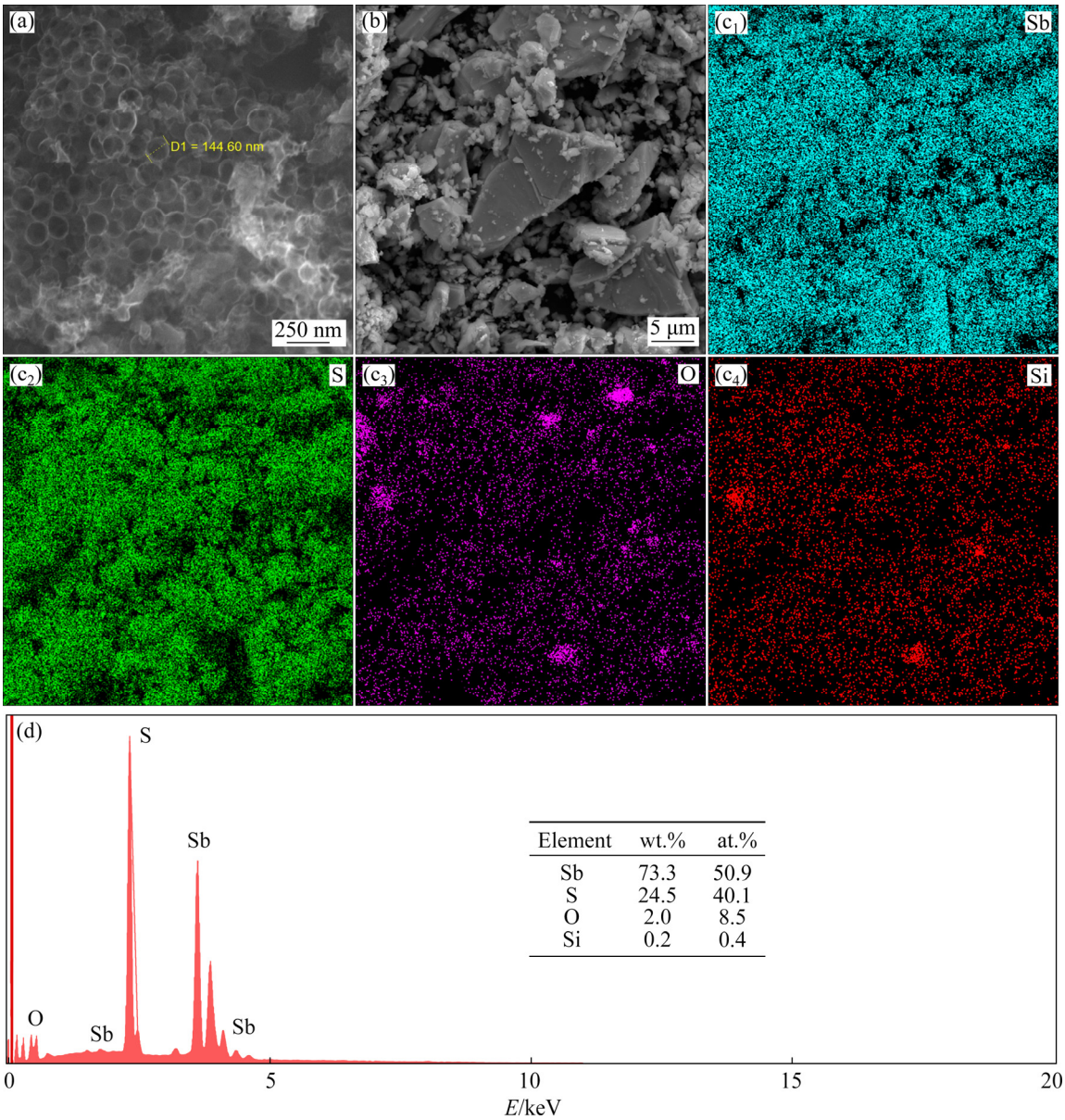

Fig. 2 SEM images of porous carbon (a) and stibnite ore (b), element mapping (c_1−c_4) and corresponding EDS spectrum of stibnite ore with Sb, S, O and Si (d)

distribution, with the large particle size of 22 μm and the small particle size about 1 μm (Fig. 2(b)). Figures 2(c, d) illustrated the existence of Si and O in bulk Sb_2S_3 ore, complying with the XRD and Raman spectra results. The bulk Sb_2S_3 ore could not directly act as active material since the micron size reduced the electrochemical performance of anode materials, as bulk structure causes tremendous volume change during the cycling, and inevitably extends the diffusion/transport path of both Li^+ and electron, which eventually destroys the electrode structure and causes serious polarization [21−24]. Thus, the electrochemical performance of the stibnite ore should be further improved.

Figures 3(a, b) present the SEM images of remodeled Sb_2S_3 ore in Melt-50% under different magnifications. After the melting treatment, the bulk Sb_2S_3 ore was remodeled to a nanorod structure with 550−600 nm in width and several microns in length. The nanorods were distributed uniformly in the porous carbon matrix. And the porous carbon had high structure stability in both ball milling and melting treatment. With the increase in Sb_2S_3 ore mass ratio, the morphology of the remodeled Sb_2S_3 ore varied. In Melt-60% (Figs. 3(c, d)), the nanorods were connected and merged to form Sb_2S_3 nanorod clusters/porous carbon. In Melt-70% (Figs. 3(e, f)), the Sb_2S_3 nanorod clusters were further merged to form bulk and micro-rod Sb_2S_3 with a particle size over 2 μm. The mergence phenomenon was more obvious, as shown in Figs. 3(g, h) (Melt-80%). The Sb_2S_3 ore particles were remodeled to microspheres in the porous carbon matrix with a larger diameter of 8.5 μm.

To investigate the chemical composition and valence states of Melt-50%, XPS measurement was employed. Figure 4(a) presents the full XPS survey spectrum, demonstrating the existence of Sb, S and C elements in Sb_2S_3 nanorods/porous-carbon composite. Figure 4(b) illustrates the high-resolution XPS of Sb 3d. The two strong peaks located at 529.88 and 539.28 eV corresponded to the banding energy of Sb $3d_{5/2}$ and $3d_{3/2}$, respectively, confirming the existence of Sb^{3+} [25]. Three intense peaks were identified in the high-resolution XPS of S 2p (Fig. 4(c)), where the peaks at 161.18 and 163.28 eV corresponded to the S $2p_{2/3}$ and S $2p_{1/2}$, demonstrating the valence state of −2; the peak at 164.88 eV was assigned to the $2p_{1/2}$ of the —C—S—C covalent bond of the thiophene-S, indicating that the Sb_2S_3 nanorods were connected to the porous carbon [26,27].

Figures 5(a, b) give TEM image, HRTEM image and EDS elemental mappings of the remodeled Sb_2S_3 nanorod in the porous carbon matrix. The Sb_2S_3 nanorod displayed the width of about 550 nm and exhibited high crystallinity with clear lattice fringes. Figures 5(c−f) show the TEM image, HRTEM image, and EDS mappings of porous carbon in Melt-50%. This carbon material showed the honeycomb-like shape with the wall

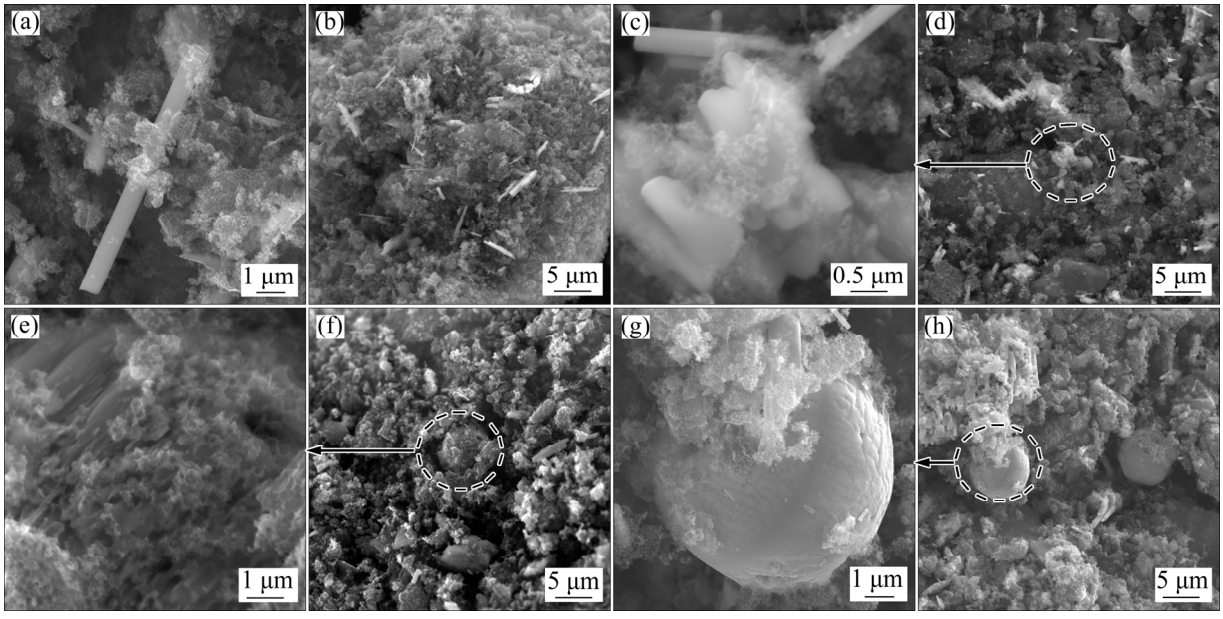

Fig. 3 SEM images of samples: (a, b) Melt-50%; (c, d) Melt-60%; (e, f) Melt-70%; (g, h) Melt-80%

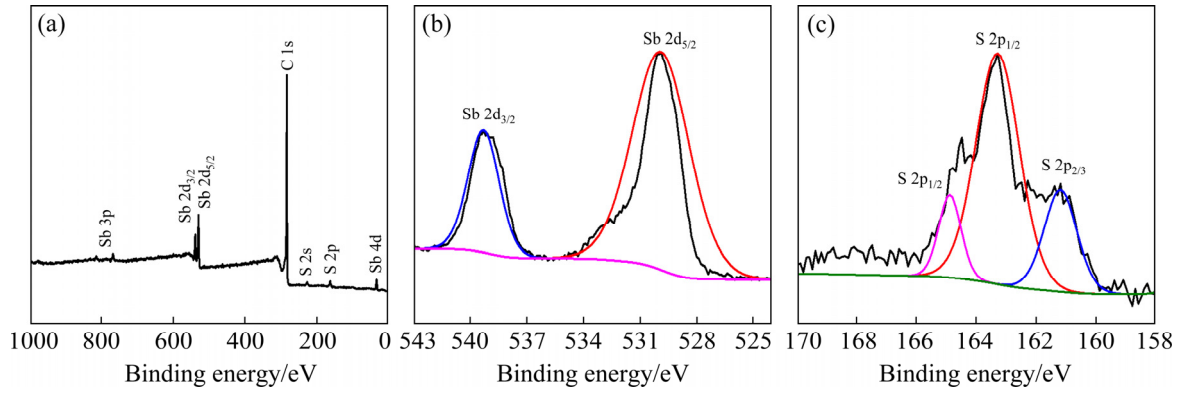

Fig. 4 XPS spectra of Sb_2S_3 nanorods/porous-carbon: (a) Survey spectrum; (b) Sb 3d spectrum; (c) S 2p spectrum

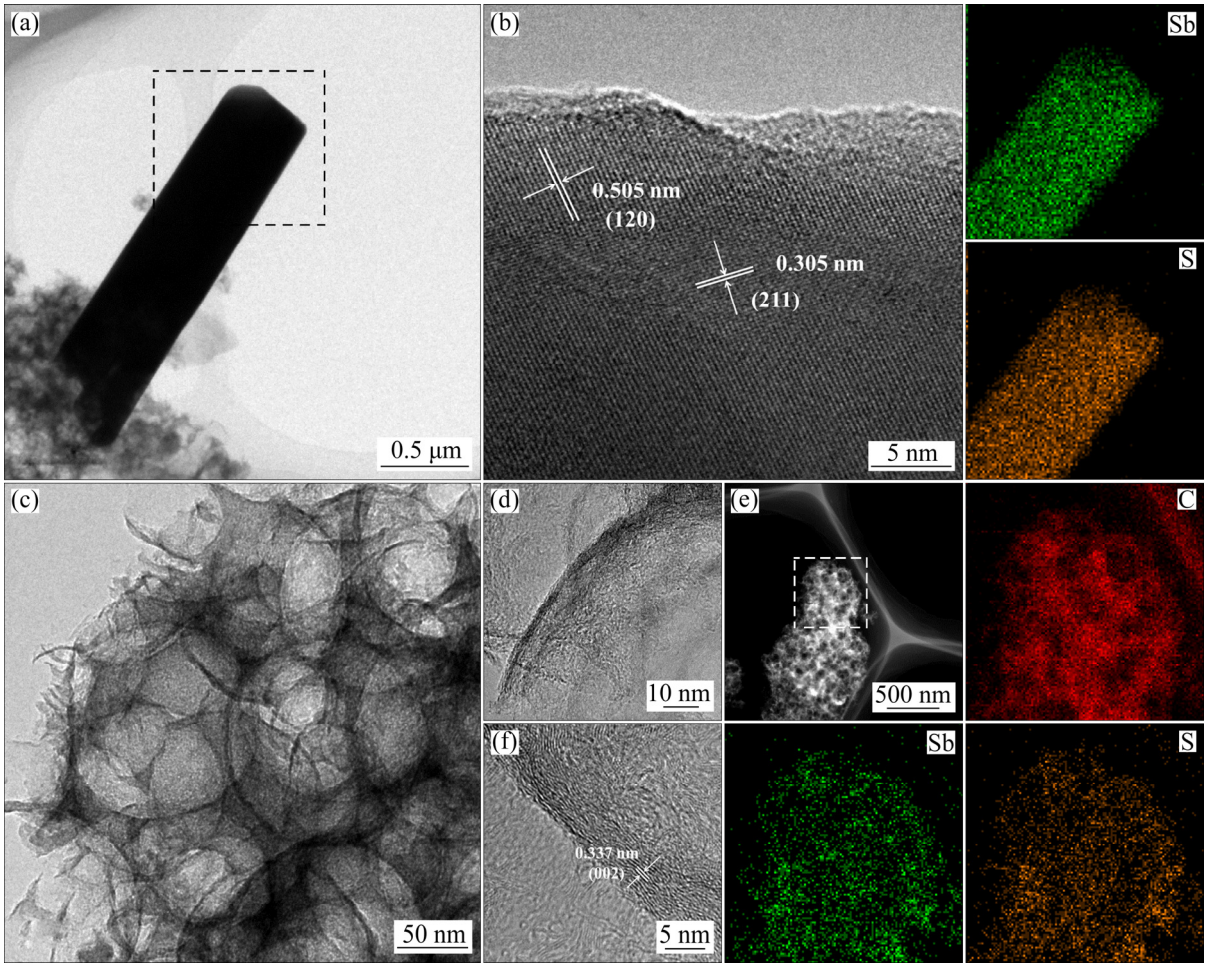

Fig. 5 TEM image of single Sb_2S_3 nanorod (a), HRTEM image and EDS elemental mappings of Sb and S of single nanorod (b); TEM image, HRTEM image and corresponding EDS elemental mappings of Sb, S and C of porous carbon in Melt-50% (c−f)

thickness of only several nanometers (Figs. 5(c, d)). Moreover, the ultrathin carbon wall exhibited a graphite structure, as confirmed by the presence of (002) interplanar spacing. The corresponding EDS elemental mapping of independent porous carbon in Melt-50% (Fig. 5(f)) indicated the existence of Sb and S, which revealed a degree of absorption of Sb_2S_3 ore by porous carbon while being melted.

3.2 Electrochemical performances

To evaluate the electrochemical properties of the obtained composites, CR2025 half-cells were

assembled with Li foil as counter electrodes. Figure 6(a) shows the initial CV curves of Melt-50% at a scan rate of 0.1 mV/s under the voltage from 0.01 to 3.0 V (vs Li^+/Li). Four peaks in both cathodic and anodic processes could be observed respectively. The two large sharp peaks in the discharge process at 1.39 and 0.54 V belonged to the reductive transformation of Sb_2S_3 to Sb and Li_2S and the alloying reaction of metallic Sb with Li^+ [28]; the corresponding two anodic peaks are

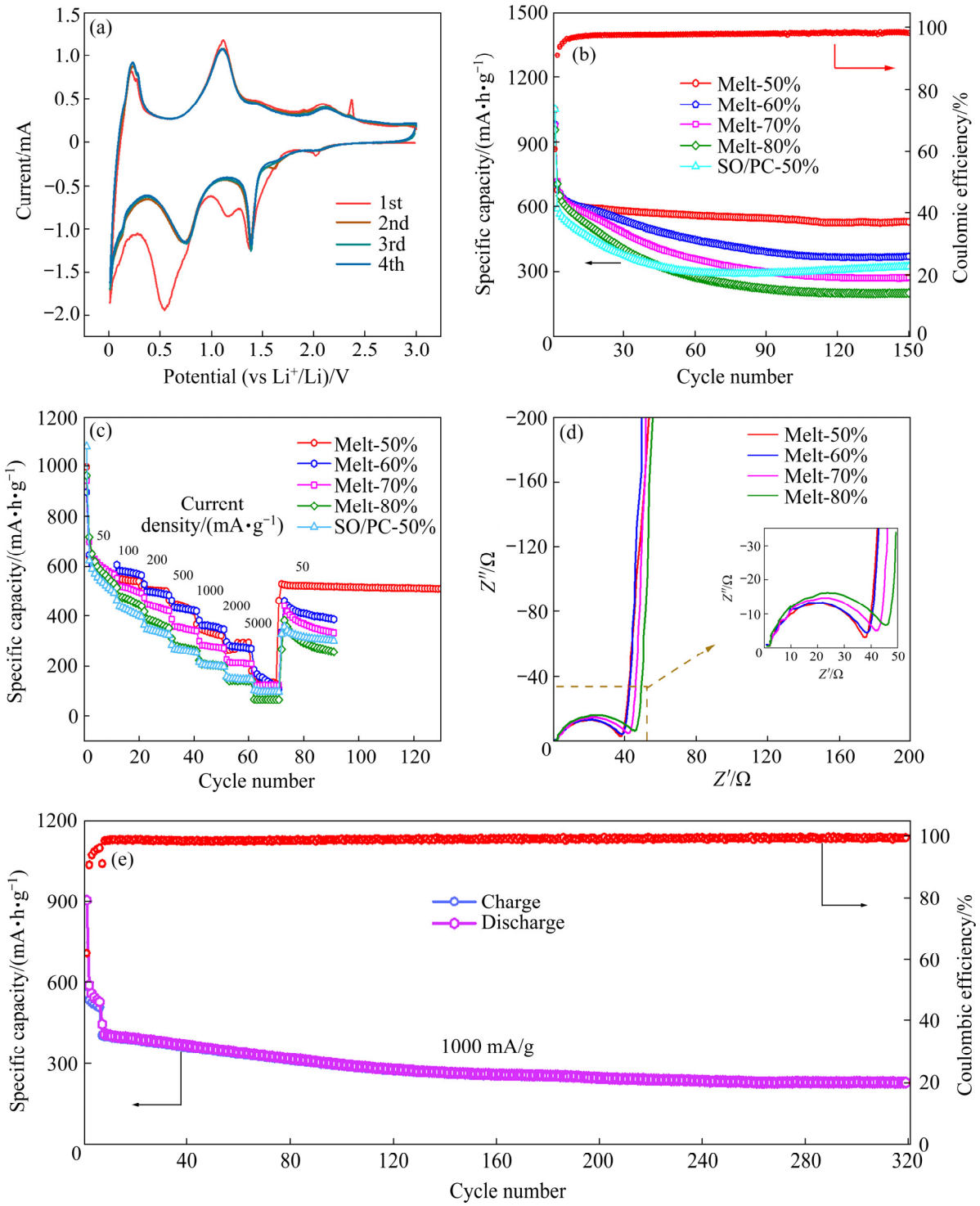

Fig. 6 Initial four CV curves of Melt-50% (a), cycling performances of Melt-50%, Melt-60%, Melt-70%, Melt-80%, and SO/PC-50%, at current density of 100 mA/g (b), rate performances of samples (c), EIS spectra of Melt-50%, Melt-60%, Melt-70% and Melt-80% (d) and cycling performance of Melt-50% at current density of 1000 mA/g (e) (The rate of *nC* was calculated by the charge−discharge time of 1/*n* hours)

located at 1.11 and 2.08 V, belonging to the dealloying reaction from Li_3Sb to Sb, and the re-formation of Sb_2S_3 by the existing Sb and Li_2S [29,30]. The peaks below 0.3 V corresponded to the reaction between graphite carbon and lithium ion [31]. An intense peak at 2.37 V during anodic scan might be the irreversible reaction caused by the impurity of Sb_2S_3 ore, which disappeared in the second scan. After the first scan, the large sharp peak at 0.54 V shifted to 0.75 V, probably related to the irreversible side reaction and the formation of solid electrolyte interface (SEI) film in the first cycle [25,32]. The CV curves overlapped well in the subsequent cycles, demonstrating the high electrochemical stability and reversibility of the Sb_2S_3 nanorods/porous-carbon anodes.

Figure 6(b) presents the corresponding cycle performances of Melt-50% and its contrast samples. At the current density of 100 mA/g, the Melt-50% electrode exhibited a high initial discharge capacity of 1049.3 mA·h/g and a reversible capacity of 637.9 mA·h/g, demonstrating an initial coulombic efficiency (ICE) of 60.79%. The relatively low coulombic efficiency could be attributed to the formation of SEI layer in the composite and irreversible side reactions by the impurities [33,34]. Melt-60%, Melt-70%, Melt-80% and SO/PC-50% electrodes exhibited initial discharge capacities of 980.9, 973.6, 955.4 and 1050.9 mA·h/g, with the corresponding ICE of 70.38%, 71.88%, 72.68% and 52.72%, respectively. Among the remodeling anodes, Melt-50% achieved higher cyclic stability and more effective capacity retention since it exhibited a discharge capacity of 530.3 mA·h/g after 150 cycles, while the others only exhibited the discharge capacity of 370.7, 272.8, 203.3 and 323.3 mA·h/g, respectively. Moreover, the nanostructures affected the rate performance of the composites (Fig. 6(c)). The Sb_2S_3 nanorods/ porous-carbon and Sb_2S_3 nanorod-clusters/ porous-carbon electrodes were suggested to achieve higher reversible capacities at the current density of 50, 100, 200, 500, 1000, 2000 and 5000 mA/g. It is noteworthy that the electrode of Melt-50% exhibited 323.6 (discharge time of 19.5 min, ~3*C*), 296.7 (6.7*C*) and 130.6 mA·h/g (40*C*) at 1000, 2000 and 5000 mA/g, respectively. Moreover, when the current density recovered to 50 mA/g, the Sb_2S_3 nanorods/porous-carbon achieved an excellent cycle stability and a retentive capacity of 511.6 mA·h/g after 130 cycles, while the others degraded fast after a high-rate cycling. EIS analysis was conducted to explore the reaction kinetics and electrochemical activities of the Melt-50%, Melt-60%, Melt-70% and Melt-80% electrodes. The corresponding Nyquist plots are given in Fig. 6(d), all of which presented low charge-transfer resistance, especially the Sb_2S_3 nanorods/porous carbon electrode, indicating the prominent electrical conductivity and the accompanying fast reaction kinetics of the composites [13]. Additionally, the cyclic stability of Sb_2S_3 nanorods/porous-carbon electrode at high current density was studied (Fig. 6(e)). After the initial activation cycles, the electrode delivered a relatively high reversible capacity of 229.2 mA·h/g even after 320 cycles, with a high coulombic efficiency up to 99.2%. The charge time was only 13.6 min, and it converted into a high rate of 4.4*C*. The excellent cyclic performance and rate capacity of Sb_2S_3 nanorods/ porous carbon were based the nanostructure of the remodeled Sb_2S_3 ore, which reduced the strain in the particles during cycle and shortened the diffusion path of Li^+ and electron. Moreover, the porous structure of the carbon matrix positively impacted the electrode since it could absorb more electrolyte and buffer the volume change of Sb_2S_3 ore nanorods. Notably, the porous carbon exhibited high conductivity for both Li^+ and electrons, which improved the reactive kinetics of the electrode.

To investigate the stability of Sb_2S_3 nanorods/porous-carbon anode, surface and cross-section SEM images before and after 150 cycles at 100 mA/g were captured (Fig. 7). It was indicated that the electrode maintained good uniformity, and there was no crack on the surface or inner of the electrode, and the thickness of the electrode did not vary significantly. Such a good structure stability of the electrode facilitates the electro-chemical performance of Sb_2S_3 nanorods/porous-carbon anodes [35], since it is capable of anchoring the active materials in the electrode and maintaining the structure of electrode [36].

4 Conclusions

(1) A novel Sb_2S_3 nanorods/porous-carbon anode material was successfully prepared by remodeling natural stibnite based on a simple melting method.

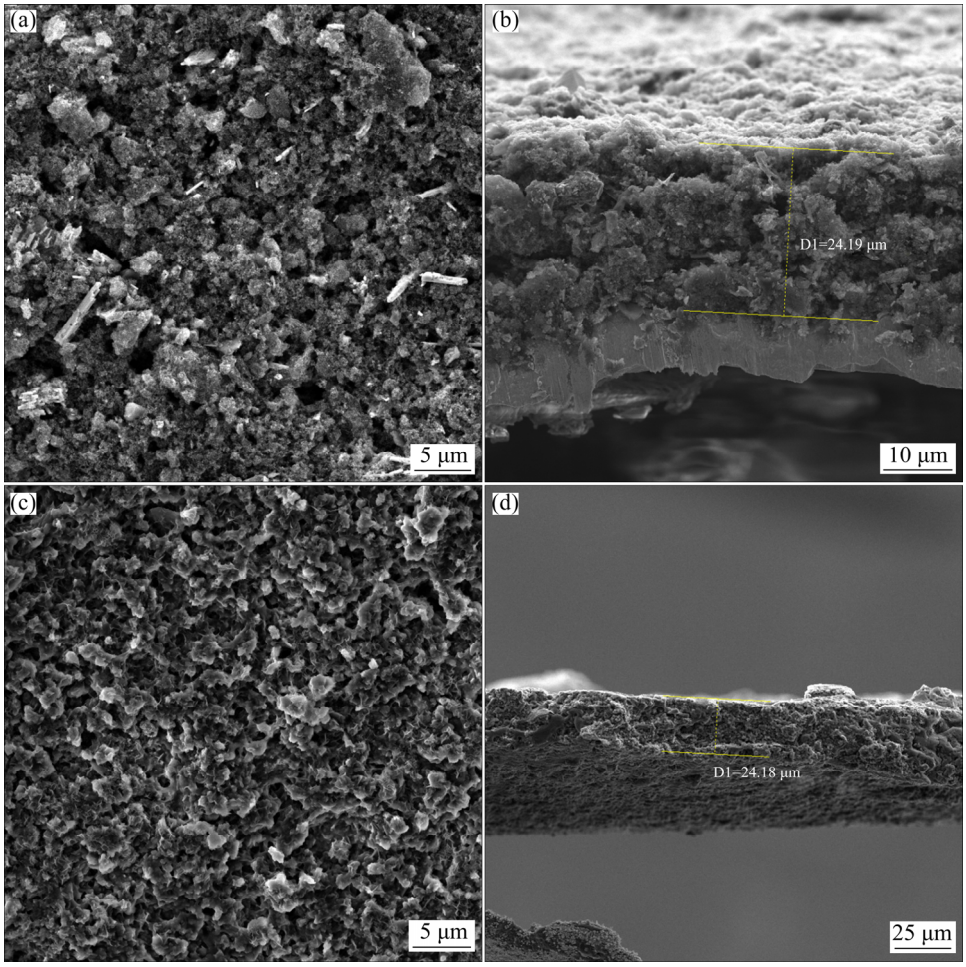

Fig. 7 Surface and cross-sectional SEM images of Melt-50% electrode before cycling (a, b), and after 150 cycles (c, d)

(2) The Sb_2S_3 nanorods/porous carbon anode achieved excellent cycling performance and a high-rate capacity in LIBs, which achieved 530.3 mA·h/g at a current density of 100 mA/g after 150 cycles, and reversible capacity of 130.6 mA·h/g at a high current density of 5000 mA/g (40*C*).

(3) The excellent electrochemical performance of Sb_2S_3 nanorods/porous carbon resulted from the nanostructures of the remodeled Sb_2S_3 ore, which reduced the strain in the particles during cycle and shortened the diffusion path of Li^+ and electron. The porous structure of the carbon matrix was capable of positively impacting the electrode since it could buffer the volume change of Sb_2S_3 nanorods and improve the reactive kinetics of the electrode.

Acknowledgments

The authors are grateful for the financial supports from the National Natural Science Foundation of China (No. 51774343).

References

[1] CAO Yu-liang, LI M, LU Jun, LIU Jun, AMINE K. Bridging the academic and industrial metrics for next-generation practical batteries [J]. Nature Nanotechnology, 2019, 14: 200−207.

[2] LI Lie-wu, WANG Li-ping, ZHANG Ming-yu, HUANG Qi-zhong, HE Ke-jian, WU Fei-xiang. Enhancement of lithium storage capacity and rate performance of Se-modified MnO/Mn_3O_4 hybrid anode material via pseudocapacitive behavior [J]. Transactions of Nonferrous Metals Society of China, 2020, 30: 1904−1915.

[3] LI Yu-qi, LU Ya-xiang, ADELHELM P, TITIRICI M M, HU Yong-sheng. Intercalation chemistry of graphite: Alkali metal ions and beyond [J]. Chemical Society Reviews, 2019, 48: 4655−4687.

[4] ZENG Jing, PENG Chao-qun, WANG Ri-chu, LIU Ya-jing, WANG Xiao-feng, LIU Jun. Preparation of dual-shell Si/TiO_2/CFs composite and its lithium storage performance [J]. Transactions of Nonferrous Metals Society of China, 2019, 29: 2384−2391.

[5] LI Xiao-chun, HE Chang-jian, ZHENG Jie, WU Dao-ning, DUAN Yu-tong, LI Yi-fei, RAO Pin-hua, TANG B, RUI Yi-chuan. Flocculent Cu caused by the Jahn–Teller effect improved the performance of Mg-MOF-74 as an anode material for lithium-ion batteries [J]. ACS Applied Materials & Interfaces, 2020, 12: 52864−52872.

[6] DONG S H, LI C X, GE X L, LI Z Q, MIAO X G, YIN L W. ZnS-Sb_2S_3@C core-double shell polyhedron structure derived from metal-organic framework as anodes for high performance sodium ion batteries [J]. ACS Nano, 2017, 11: 6474−6482.

[7] ZHANG Zhen-dong, ZHAO Jia-chang, XU Mei-lan, WANG Hong-xia, GONG Yan-mei, XU Jing-li. Facile synthesis of Sb_2S_3/MoS_2 heterostructure as anode material for sodium-ion batteries [J]. Nanotechnology, 2018, 29: 335401.

[8] CHAI Wen-wen, YANG Fan, YIN Wei-hao, YOU Shun-zhang, WANG Ke, YE Wen-kai, RUI Yi-chuan, TANG Bo-he-jin. Bi_2S_3/C nanorods as efficient anode materials for lithium-ion batteries [J]. Dalton Transactions, 2019, 48: 1906−1914.

[9] YAO S S, CUI J, LU Z H, XU Z L, QIN L, HUANG J Q, SADIGHI Z, CIUCCI F, KIM J K. Unveiling the unique phase transformation behavior and sodiation kinetics of 1D van der Waals Sb_2S_3 anodes for sodium ion batteries [J]. Advanced Energy Materials, 2017, 7: 11.

[10] LUO Wen, LI Feng, GAUMET J J, MAGRI P, DILIBERTO S, ZHOU Liang, MAI Li-qiang. Bottom-up confined synthesis of nanorod-in-nanotube structured Sb@N−C for durable lithium and sodium storage [J]. Advanced Energy Materials, 2018, 8: 1703237.

[11] WANG Qi, LIU Fang-yang, WANG Li, JIANG Liang-xing, WANG Qi-yu, HONG Bo, LAI Yan-qing. Towards fast and low cost Sb_2S_3 anode preparation: A simple vapor transport deposition process by directly using antimony sulfide ore as raw material [J]. Scripta Materialia, 2019, 173: 75−79.

[12] LI J, QIN F R, ZHANG L Y, ZHANG K, LI Q, LAI Y Q, ZHANG Z A, Fang J. Mesoporous carbon from biomass: One-pot synthesis and application for Li−S batteries [J]. Journal of Materials Chemistry A, 2014, 2: 13916−13922.

[13] ZHONG Yu, CHAO Dong-liang, DENG Sheng-jue, ZHAN Ji-ye, FANG Ru-Yi, XIA Yang, WANG Ya-dong, WANG Xiu-li, XIA Xin-hui, TU Jiang-ping. Confining sulfur in integrated composite scaffold with highly porous carbon fibers/vanadium nitride arrays for high-performance lithium–sulfur batteries [J]. Advanced Functional Materials, 2018, 28: 1706391.

[14] YANG Kai, GAO Qiu-ming, TAN Yan-li, TIAN Wei-qian, QIAN Wei-wei, ZHU Li-hua, YANG Chun-xiao. Biomass-derived porous carbon with micropores and small mesopores for high-performance lithium−sulfur batteries [J]. Chemistry−A European Journal, 2016, 22: 3239−3244.

[15] LI G, SUN J H, HOU W P, JIANG S D, HUANG Y, GENG J X. Three-dimensional porous carbon composites containing high sulfur nanoparticle content for high-performance lithium−sulfur batteries [J]. Nature Communications, 2016, 7: 10.

[16] PARIZE R, COSSUET T, CHAIX P O, ROUSSEL H, APPERT E, CONSONNI V. In situ analysis of the crystallization process of Sb_2S_3 thin films by Raman scattering and X-ray diffraction [J]. Materials & Design, 2017, 121: 1−10.

[17] HWANG S M, KIM J, KIM Y, KIM Y. Na-ion storage performance of amorphous Sb_2S_3 nanoparticles: Anode for Na-ion batteries and seawater flow batteries [J]. Journal of Materials Chemistry A, 2016, 4: 17946−17951.

[18] ZHOU X Z, ZHANG Z F, LU X F, LV X Y, MA G F, WANG Q T, LEI Z Q. Sb_2O_3 Nanoparticles anchored on graphene sheets via alcohol dissolution- reprecipitation method for excellent lithium-storage properties [J]. ACS Applied Materials & Interfaces, 2017, 9: 34927−34936.

[19] LI Hai, QIAN Kun, QIN Xian-ying, LIU Dong-qing, SHI Rui-ying, RAN Ai-hua, HAN Cui-ping, HE Yan-Bing, KANG Fei-yu, LI Bao-hua. The different Li/Na ion storage mechanisms of nano Sb_2O_3 anchored on graphene [J]. Journal of Power Sources, 2018, 385: 114−121.

[20] MAKRESKI P, PETRUŠEVSKI G, UGARKOVIĆ S, JOVANOVSKI G. Laser-induced transformation of stibnite (Sb_2S_3) and other structurally related salts [J]. Vibrational Spectroscopy, 2013, 68: 177−182.

[21] BALAYA P. Size effects and nanostructured materials for energy applications [J]. Energy & Environmental Science, 2008, 1: 645−654.

[22] WANG Yong-gang, LI Hui-qiao, HE Ping, HOSONO Ei-ji, ZHOU Hao-shen. Nano active materials for lithium-ion batteries [J]. Nanoscale, 2010, 2: 1294−1305.

[23] MANTHIRAM A, VADIVEL M A, SARKAR A, MURALIGANTH T. Nanostructured electrode materials for electrochemical energy storage and conversion [J]. Energy & Environmental Science, 2008, 1: 621−638.

[24] KANG B, CEDER G. Battery materials for ultrafast charging and discharging [J]. Nature, 2009, 458: 190−193.

[25] DONG Yu-cheng, YANG Shi-liu, ZHANG Zhen-yu, LEE Jong-Min, ZAPIEN J A. Enhanced electrochemical performance of lithium ion batteries using Sb_2S_3 nanorods wrapped in graphene nanosheets as anode materials [J]. Nanoscale, 2018, 10: 3159−3165.

[26] DONG Y R, JIANG H, DENG Z N, HU Y J, LI C Z. Synthesis and assembly of three-dimensional MoS_2/rGO nanovesicles for high-performance lithium storage [J]. Chemical Engineering Journal, 2018, 350: 1066−1072.

[27] YAN Yang, YIN Ya-xia, XIN Sen, GUO Yu-guo, WAN Li-jun. Ionothermal synthesis of sulfur-doped porous carbons hybridized with graphene as superior anode materials for lithium-ion batteries [J]. Chemical Communications, 2012, 48: 10663−10665.

[28] PARK C M, HWA Y, SUNG N E, SOHN H J. Stibnite (Sb_2S_3) and its amorphous composite as dual electrodes for rechargeable lithium batteries [J]. Journal of Materials Chemistry, 2010, 20: 1097−1102.

[29] PRIKHODCHENKO P V, GUN J, SLADKEVICH S, MIKHAYLOV A A, LEV O, TAY Y Y, BATABYAL S K, YU D Y W. Conversion of Hydroperoxoantimonate coated graphenes to Sb_2S_3@graphene for a superior lithium battery anode [J]. Chemistry of Materials, 2012, 24: 4750−4757.

[30] YI Zheng, HAN Qi-gang, CHENG Yong, WU Yao-ming, WANG Li-min. Facile synthesis of symmetric bundle-like Sb_2S_3 micron-structures and their application in lithium-ion battery anodes [J]. Chemical Communications, 2016, 52:

7691−7694.
[31] WU Ze, CHENG Xin-qun, TIAN Dong, GAO Tian-tian, HE Wei-dong, YANG Chun-hui. SiOC nanolayers directly-embedded in graphite as stable anode for high-rate lithium ion batteries [J]. Chemical Engineering Journal, 2019, 375: 121997.
[32] ZHAN Jing, XU Chang-fan, LONG Yi-yu, LI Qi-hou. Preparation and electrochemical performance of nitrogen-doped carbon-coated $Bi_2Mn_4O_{10}$ anode materials for lithium-ion batteries [J]. Transactions of Nonferrous Metals Society of China, 2020, 30: 2188−2199.
[33] ZHU Y Y, NIE P, SHEN L F, DONG S Y, SHENG Q, LI H S, LUO H F, ZHANG X G. High rate capability and superior cycle stability of a flower-like Sb_2S_3 anode for high-capacity sodium ion batteries [J]. Nanoscale, 2015, 7: 3309−3315.
[34] CUI C Y, WEI Z X, XU J T, ZHANG Y Q, LIU S H, LIU H K, MAO M L, WANG S Y, MA J M, DOU S X. Three-dimensional carbon frameworks enabling MoS_2 as anode for dual ion batteries with superior sodium storage properties [J]. Energy Storage Materials, 2018, 15: 22−30.
[35] LUO Yan-zhu, HUANG De-kang, LIANG Chen-nan, WANG Pei, HAN Kang, WU Bu-ke, CAO Fei-fei, MAI Li-qiang, CHEN Hao. Fe_2VO_4 hierarchical porous microparticles prepared via a facile surface solvation treatment for high-performance lithium and sodium storage [J]. Small, 2019, 15: 1804706.
[36] ZHU Shan-shan, ZHOU Jian-bin, GUAN Yong, CAI Wen-long, ZHAO Ying-yue, ZHU Yuan-chao, ZHU Lin-qin, ZHU Yong-chun, QIAN Yi-tai. Hierarchical graphene-scaffolded silicon/graphite composites as high performance anodes for lithium-ion batteries [J]. Small, 2018, 14: 1802457.

以天然辉锑矿为原料制备 Sb_2S_3 纳米线/多孔碳复合物作为高性能锂离子电池负极材料

汪 齐[1]，赖延清[1]， 刘芳洋[1]，蒋良兴[1]，贾 明[1,2]，王熙伦[3]

1. 中南大学 冶金与环境学院，长沙 410083；
2. 湖南城市学院 全固态储能材料与器件湖南省重点实验室，益阳 413000；
3. 益阳市华昌锑业有限公司，益阳 413000

摘 要：为了避免目前锂离子电池负极材料制造所使用的高纯试剂和高能耗，采用简单熔融法制备以多孔碳为基体的 Sb_2S_3 纳米线/多孔碳复合负极材料。得益于活性材料 Sb_2S_3 的纳米结构和多孔碳的协同作用，复合负极材料在 100 mA/g 下循环 150 次后仍可实现 530.3 mA·h/g 的高可逆容量，在 5000 mA/g 下循环 320 次仍可获得 130.6 mA·h/g 的容量。研究结果揭示直接利用辉锑矿作为先进锂离子电池负极材料的可能性和实用性。

关键词：锂离子电池；辉锑矿；经济制备；纳米结构负极材料

(Edited by Bing YANG)